

Northumbria Research Link

Citation: Karamelas, Konstantinos, McLaughlin, James, Botha, Gert and Regnier, Stephane (2023) Oscillatory Reconnection as a Plasma Diagnostic in the Solar Corona. The Astrophysical Journal, 943 (2). p. 131. ISSN 0004-637X

Published by: IOP Publishing

URL: <https://doi.org/10.3847/1538-4357/acac90> <<https://doi.org/10.3847/1538-4357/acac90>>




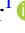
This version was downloaded from Northumbria Research Link: <https://nrl.northumbria.ac.uk/id/eprint/51314/>

Northumbria University has developed Northumbria Research Link (NRL) to enable users to access the University's research output. Copyright © and moral rights for items on NRL are retained by the individual author(s) and/or other copyright owners. Single copies of full items can be reproduced, displayed or performed, and given to third parties in any format or medium for personal research or study, educational, or not-for-profit purposes without prior permission or charge, provided the authors, title and full bibliographic details are given, as well as a hyperlink and/or URL to the original metadata page. The content must not be changed in any way. Full items must not be sold commercially in any format or medium without formal permission of the copyright holder. The full policy is available online: <http://nrl.northumbria.ac.uk/policies.html>

This document may differ from the final, published version of the research and has been made available online in accordance with publisher policies. To read and/or cite from the published version of the research, please visit the publisher's website (a subscription may be required.)



Oscillatory Reconnection as a Plasma Diagnostic in the Solar Corona

Konstantinos Karamelas^{1,2} , James A. McLaughlin¹ , Gert J. J. Botha¹ , and Stéphane Régnier¹ ¹ Department of Mathematics, Physics and Electrical Engineering, Northumbria University, Newcastle upon Tyne, NE1 8ST, UK; kostas.karamelas@kuleuven.be² Centre for mathematical Plasma Astrophysics, Department of Mathematics, KU Leuven, Celestijnenlaan 200B bus 2400, B-3001 Leuven, Belgium

Received 2022 November 1; revised 2022 December 6; accepted 2022 December 15; published 2023 February 2

Abstract

Oscillatory reconnection is a relaxation process in magnetized plasma, with an inherent periodicity that is exclusively dependent on the properties of the background plasma. This study focuses on the seismological prospects of oscillatory reconnection in the solar corona. We perform three sets of parameter studies (for characteristic coronal values of the background magnetic field, density, and temperature) using the PLUTO code to solve the fully compressive, resistive MHD equations for a 2D magnetic X-point. From each parameter study, we derive the period of the oscillatory reconnection. We find that this period is inversely proportional to the characteristic strength of the background magnetic field and the square root of the initial plasma temperature, while following a square root dependency upon the equilibrium plasma density. These results reveal an inverse proportionality between the magnitude of the Alfvén speed and the period, as well as the background speed of sound and the period. Furthermore, we note that the addition of anisotropic thermal conduction only leads to a small increase in the mean value for the period. Finally, we establish an empirical formula that gives the value for the period in relation to the background magnetic field, density, and temperature. This gives us a quantified relation for oscillatory reconnection, to be used as a plasma diagnostic in the solar corona, opening up the possibility of using oscillatory reconnection for coronal seismology.

Unified Astronomy Thesaurus concepts: [Magnetohydrodynamics \(1964\)](#); [Solar magnetic reconnection \(1504\)](#); [Solar coronal seismology \(1994\)](#); [Solar coronal waves \(1995\)](#); [Magnetohydrodynamical simulations \(1966\)](#)

1. Introduction

Oscillatory reconnection is a physical phenomenon characterized by a series of reconnection events (Parker 1957; Sweet 1958; Petschek 1964) that take place alongside periodic changes in the magnetic connectivity of a perturbed magnetic field. The process was identified for the first time in Craig & McClymont (1991), during the study of the relaxation of a 2D X-point. One important characteristic of oscillatory reconnection is that the periodicity is not imposed by an external driver, rather it is an inherent property of the relaxation process.

Over recent years, a number of numerical studies have been conducted regarding oscillatory reconnection. McLaughlin et al. (2009) studied the mechanism for a 2D magnetic X-point in a cold plasma, solving the fully compressible resistive MHD equations. Using an external fast magnetoacoustic pulse, they initiated oscillatory reconnection by perturbing a magnetic X-point. This study identified many properties of this mechanism, like the periodic changes in the resulting current sheet orientation with the respective changes in connectivity, and the formation of both fast and slow oblique magnetic shocks. Thurgood et al. (2017) later expanded the results of the previous study for a 3D null point, also reporting the generation of MHD waves. Oscillatory reconnection has also been studied for a realistic solar atmosphere, as a result of flux rope emergence (Murray et al. 2009; McLaughlin et al. 2012b), while other studies revolved around the effects of resistivity, initial perturbation amplitude, and the length of the initial current sheet on the period of the reconnection process (McLaughlin et al. 2012a; Thurgood et al. 2018a, 2018b,

2019). Stewart et al. (2022) reported the onset of oscillatory reconnection and the generation of waves through the coalescence of two cylindrical flux ropes, while Sabri et al. (2020) reported the development of the plasmoid instability in a magnetic O-point and the resulting manifestation of plasmoid-mediated quasi-oscillatory magnetic reconnection. The results of McLaughlin et al. (2009) have recently been expanded for a hot coronal plasma in Karamelas et al. (2022a), studying the relation between the oscillation period and the strength of the background magnetic field, while also taking into account the effects of anisotropic thermal conduction. A following study (Karamelas et al. 2022b) reported for the first time the independence between the type and strength of the perturbing wave pulse and the frequency of the resulting oscillatory reconnection in a hot coronal plasma. These two studies have produced encouraging results regarding the possibility of using oscillatory reconnection as a new tool for coronal seismology.

Magnetic reconnection can cause the dissipation of the magnetic field and electric current, leading to the acceleration of particles, ejection of mass, and heating through the generation of shocks. As such, it is considered the main mechanism behind solar flares (e.g., Shibata & Magara 2011; Jelinek et al. 2015), while the ubiquitous null points in the solar atmosphere (Galsgaard & Nordlund 1997; Brown & Priest 2001; Longcope 2005; Régnier et al. 2008), where reconnection can take place, are consequently considered preferential locations of the manifestation of flares (e.g., Murawski et al. 2011). Over the years, oscillatory reconnection has been proposed as a driving force behind observed phenomena like quasi-periodic pulsations (QPPs) of solar flares Kupriyanova et al. 2016; Van Doorsselaere et al. 2016; Pugh et al. 2017; Yuan et al. 2019; Li et al. 2020a, 2020b; Hayes et al. 2020; Clarke et al. 2021; Li et al. 2021; Li & Chen 2022; Li et al. 2022; Shi et al. 2022) and stellar flares

(e.g., Guarcello et al. 2019; Broomhall et al. 2019; Notsu et al. 2019; Vida et al. 2019; Jackman et al. 2019; Mancuso et al. 2020; Ramsay et al. 2021). The mechanism is included in reviews summarizing our current knowledge of QPPs and the proposed mechanisms behind them, such as those of McLaughlin et al. (2018), Kupriyanova et al. (2020), and Zimovets et al. (2021). In particular, there are many examples from QPP observations (see the histogram in McLaughlin et al. 2018, and its corresponding online catalog), with reported periods close to those derived from the studies of Karampelas et al. (2022a) and Karampelas et al. (2022b), for the plasma conditions considered in those studies.

Connection has also been proposed between oscillatory reconnection and quasi-periodic flows, like those associated with spicules (e.g., De Pontieu & McIntosh 2010; De Pontieu et al. 2011; Samanta et al. 2019; Yurchyshyn et al. 2020), as well as with observed periodicities in breakout current sheets at the base of jets (Hong et al. 2019). Mandal et al. (2022) reported a highly dynamic small-scale jet in a polar coronal hole, and proposed oscillatory reconnection as a possible driving mechanism behind the observed repetitive outflows. McLaughlin et al. (2012b) were able to reproduce such observed periodic outflows through oscillatory reconnection in a 2D flux emergence model. The resulting periods from that model had a very good match with those reported from wavelet analysis in Mandal et al. (2022), although the latter showed no significant power at the 99% confidence level, preventing them to characterize the outflows as periodic, but merely repetitive. Observational signatures of chromospheric jets by periodic reconnection events have also been reported in simulations by Heggland et al. (2009), although, the periodicity was attributed to the continuous driving rather than being inherent to the system. Oscillatory reconnection has also been considered as a possible mechanism behind the creation of an observed quasi-periodic fast-propagating (QFP) magnetosonic wave from the eruption of a magnetic flux rope (Shen et al. 2018), as well as behind the formation and disappearance of a small-scale magnetic flux rope consisting of new loops formed by the reconnection events (Xue et al. 2019). Zhang et al. (2014) reported oscillatory (or reciprocity) magnetic reconnection in observations of coronal bright points (CBPs), while reversals of an elongated current sheet in a recent numerical 2D CBP model have been attributed to oscillatory reconnection (Nobrega-Siverio & Moreno-Insertis 2022). Finally, recent observations by the Parker Solar Probe could also be attributed to oscillatory reconnection (e.g., Bale et al. 2016; Kasper et al. 2019; Bale et al. 2019), like Alfvénic spikes (He et al. 2021) and periodicities correlated with Type III radio bursts (Cattell et al. 2021).

In this paper, we further investigate oscillatory reconnection in a hot coronal plasma and explore its potential for utilizing oscillatory reconnection as a tool for coronal seismology. We expand the results of Karampelas et al. (2022a) through a series of parameter studies for different characteristic strengths of the magnetic field, equilibrium plasma density, and initial plasma temperature, for a 2D magnetic X-point. Like in Karampelas et al. (2022a) and Karampelas et al. (2022b), we explore these cases both in the absence and presence of anisotropic thermal conduction. In Section 2, we present our physical domain, the code used to solve the fully compressible MHD equations, and the numerical schemes utilized, while we present the results of the parameter studies in the respective subsection in Section 3.

Finally, our conclusions and a general discussion are given in Section 4.

2. Numerical Setup

2.1. Numerical Scheme

For the numerical studies below, we solve the 2D compressible resistive MHD equations in Cartesian coordinates, in the absence of gravity (see Section 2.1 in Karampelas et al. 2022a), using the PLUTO code (Mignone et al. 2007, 2012). Like in our past studies (Karampelas et al. 2022a, 2022b), we employ the fifth-order monotonicity preserving scheme (MP5) for the spatial integration and the third-order Runge–Kutta method for the time integration. To satisfy the solenoidal constraint of the magnetic field ($\nabla \cdot \mathbf{B} = 0$), we use the Constrained Transport method implemented in the code.

In these simulations, we also consider setups where we introduce anisotropic thermal conduction. The values for the parallel and perpendicular thermal conduction coefficients (in $\text{J s}^{-1} \text{K}^{-1} \text{m}^{-1}$), as calculated from the Spitzer conductivity (Orlando et al. 2008), are given below:

$$\kappa_{\parallel} = 5.6 \times 10^{-12} T^{\frac{5}{2}}, \quad (1)$$

$$\kappa_{\perp} = 3.3 \times 10^{-21} \frac{n_{\text{H}}^2}{\sqrt{TB^2}}, \quad (2)$$

where κ_{\parallel} , κ_{\perp} , and the hydrogen number density n_{H} , temperature T , and magnetic field B are all given in SI units.³ The effects of saturation are also taken into account for very large temperature gradients. The corresponding source term ($\nabla \cdot \mathbf{F}_c$) in the energy equation varies between the classical ($\mathbf{F}_{\text{class}}$) and saturated thermal conduction (\mathbf{F}_{sat}):

$$\nabla \cdot \mathbf{F}_c = \nabla \cdot \left(\frac{F_{\text{sat}}}{F_{\text{sat}} + |\mathbf{F}_{\text{class}}|} \mathbf{F}_{\text{class}} \right), \quad (3)$$

$$\mathbf{F}_{\text{class}} = \kappa_{\parallel} \hat{\mathbf{b}} (\hat{\mathbf{b}} \cdot \nabla T) + \kappa_{\perp} [\nabla T - \hat{\mathbf{b}} (\hat{\mathbf{b}} \cdot \nabla T)], \quad (4)$$

$$F_{\text{sat}} = 5 \phi \rho V_{\text{S,iso}}^3, \quad (5)$$

where $V_{\text{S,iso}} = \sqrt{p/\rho}$ is the isothermal speed of sound, $\hat{\mathbf{b}} = \mathbf{B}/|\mathbf{B}|$ is the unit vector in the direction of the magnetic field, and ϕ is a free code parameter (with a default value of 0.3). For zero magnetic field, \mathbf{F}_c reduces to $\mathbf{F}_c = \kappa_{\parallel} \nabla T$.

During this analysis, we work in code units $U = U_{\text{ph}} U_0^{-1}$, with U_{ph} being the physical quantities and U_0 the normalization unit. The constants U_0 are characteristic values, chosen for solar coronal plasma. We consider the unit length $L_0 = 1$ Mm, unit density $\rho_0 = 10^{-12} \text{ kg m}^{-3}$, and unit velocity $v_0 = 1.29 \times 10^5 \text{ m s}^{-1}$, equal to $V_{\text{S}}/\sqrt{\gamma}$ for coronal plasma at 1 MK. We also take the unit temperature $T_0 = 1$ MK. The characteristic magnetic field and unit time are, respectively, $B_0 = \sqrt{\mu \rho_0 v_0^2} = 1.44 \text{ G}$ and $t_0 = L_0/v_0 = 7.78 \text{ s}$.

Since we want to solve the resistive MHD equations, we take the magnetic diffusivity in code units as $\eta = R_m^{-1} = 10^{-5}$, where $R_m = (v_0 L_0)/\eta = 10^5$ is the magnetic Reynolds number,

³ In cgs, the thermal conduction coefficients (in $\text{erg s}^{-1} \text{K}^{-1} \text{cm}^{-1}$) are given as $\kappa_{\parallel} = 5.6 \times 10^{-7} T^{\frac{5}{2}}$ and $\kappa_{\perp} = 3.3 \times 10^{-16} \frac{n_{\text{H}}^2}{\sqrt{TB^2}}$.

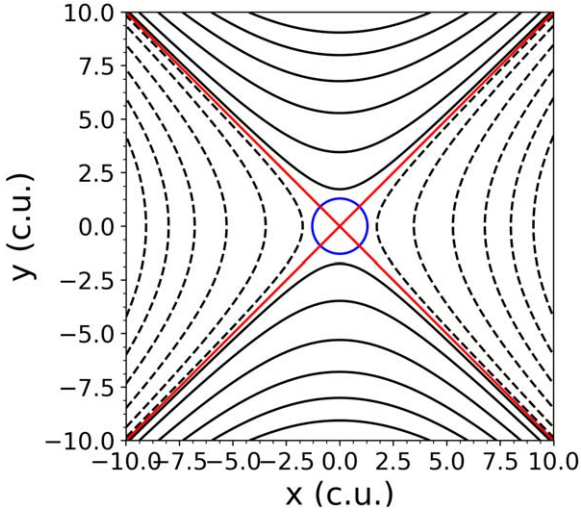


Figure 1. Magnetic field lines of the unperturbed X-point, where the black solid and dashed lines depict the regions of opposing polarity. The separatrices (red solid lines) and the equipartition layer for a 1 MK coronal plasma (blue circle) are also included.

assuming that the typical length and velocity scales of our system are, respectively, L_0 and v_0 . Due to the finite size of our grid, our code also faces the effects of the *effective* numerical diffusivity, which prevents us from using R_m values closer to those expected in the solar corona. Through a parameter study, this numerical diffusivity is estimated to be on the order of 10^{-6} – 10^{-5} .

2.2. Initial Setup

This numerical study focuses on the perturbations of a 2D magnetic X-point. Similarly to Karampelas et al. (2022a), the equilibrium magnetic field is defined in physical units as

$$\mathbf{B} = \frac{B_0}{L_0}(y, x, 0). \quad (6)$$

In Equation (6), B_0 is the characteristic magnetic field strength, and L_0 is the characteristic length scale of the magnetic field variations. A visual depiction of the magnetic field is shown in Figure 1, where the black solid and dashed lines depict the magnetic field lines in the regions with opposite polarities; the separatrices are in red. From Equation (6) we can also see that the magnitude of the magnetic field is proportional to the radius $r = \sqrt{x^2 + y^2}$.

We consider uniform equilibrium values for the density and temperature across the physical domain, obtaining a uniform initial speed of sound

$$V_S = \sqrt{\gamma} V_{S,\text{iso}} = \sqrt{\gamma p / \rho} = \sqrt{\gamma R T}, \quad (7)$$

where $\gamma = 5/3$ is the ratio of the specific heat, and R is the specific gas constant. This also results in an increasing Alfvén speed of

$$V_A = \frac{B}{\sqrt{\mu_0 \rho}} = \frac{B_0}{L_0} \frac{r}{\sqrt{\mu_0 \rho}}, \quad (8)$$

(μ_0 is the magnetic permeability of vacuum) as we move away from the X-point. Additionally, the choice of a uniform initial density distribution prevents the development of phase mixing in our setups (e.g., Heyvaerts & Priest 1983). Figure 1 also

depicts the equipartition layer, i.e., the layer where the ratio of V_A over V_S equals 1. Given that the initial V_S is constant in our setups, and V_A is proportional to the magnitude of the magnetic field, and thus the radius, the equipartition layer will initially be a circle of radius, r_{eq} , where

$$r_{\text{eq}} = \frac{L_0}{B_0} \sqrt{\frac{\gamma \rho R T}{\mu_0}}. \quad (9)$$

From Equation (9) we can see that the initial radius of the equipartition layer in our setups will be defined by the values of the initial uniform plasma temperature and density, and by the characteristic strength of the magnetic field.

In order to initiate oscillatory reconnection at the X-point, we use a circular fast magnetoacoustic pulse (mentioned as a Ring driver in Karampelas et al. (2022b)) to perturb the magnetic field from its equilibrium state. The horizontal components of the velocity pulse, as shown in Figure 2, are calculated as follows:

$$v_x = (v_{\parallel} B_x + v_{\perp} B_y) / (B_x^2 + B_y^2), \quad (10)$$

$$v_y = (v_{\parallel} B_x - v_{\perp} B_y) / (B_x^2 + B_y^2), \quad (11)$$

where $v_{\perp} = (\mathbf{v} \times \mathbf{B}) \cdot \hat{\mathbf{z}}$ is a quantity related to the velocity component perpendicular to the magnetic field lines and $v_{\parallel} = \mathbf{v} \cdot \mathbf{B}$ is a quantity related to the velocity component parallel to the magnetic field lines. Following Karampelas et al. (2022a), we consider a fast magnetoacoustic wave pulse (in code units) of the form

$$v_{\perp}(t=0) = \frac{1}{0.2\sqrt{2\pi}} \exp\left(-0.5 \frac{(r-5)^2}{0.2}\right), \quad (12)$$

$$v_{\parallel}(t=0) = 0. \quad (13)$$

2.3. Domain and Boundary Conditions

Our setup consists of a square domain with a structured uniform grid with a range of $(x, y) \in [-10, 10]$ in code units, and a resolution of 1801×1801 grid points. We use reflective boundaries for the velocity components (v_x, v_y), so that no flows can cross the boundary and disrupt the initial equilibrium. To prevent the accumulation of heat at the boundaries, once thermal conduction is switched on, we fix pressure and density at the boundaries to their initial values. In order to keep the current density at the edges or our domain from getting artificial values due to boundary effects, we take zero-gradient boundary conditions for the magnetic field components (of the form $B_i - B_{i-1} = B_{i+1} - B_i$).

Following Karampelas et al. (2022b), we take steps to minimize the amount of reflected waves from the boundaries returning to the null point. Our first step is to deal with the outward propagating velocity pulse that emerges from the splitting of the initial velocity annulus, as can be seen in Figure 3 at $t = 0.2 t_0$. We do so after the start of each simulation, by turning the value of the velocity components to zero for a region with a radius of $r \geq 7$.

The second step is to create a numerical dissipation scheme away from the null point, with the purpose of reducing the kinetic energy of the waves in that region. To that end, we divide each velocity component by a dissipation coefficient of $n_d > 1$, for each iteration. The relation for the coefficient is

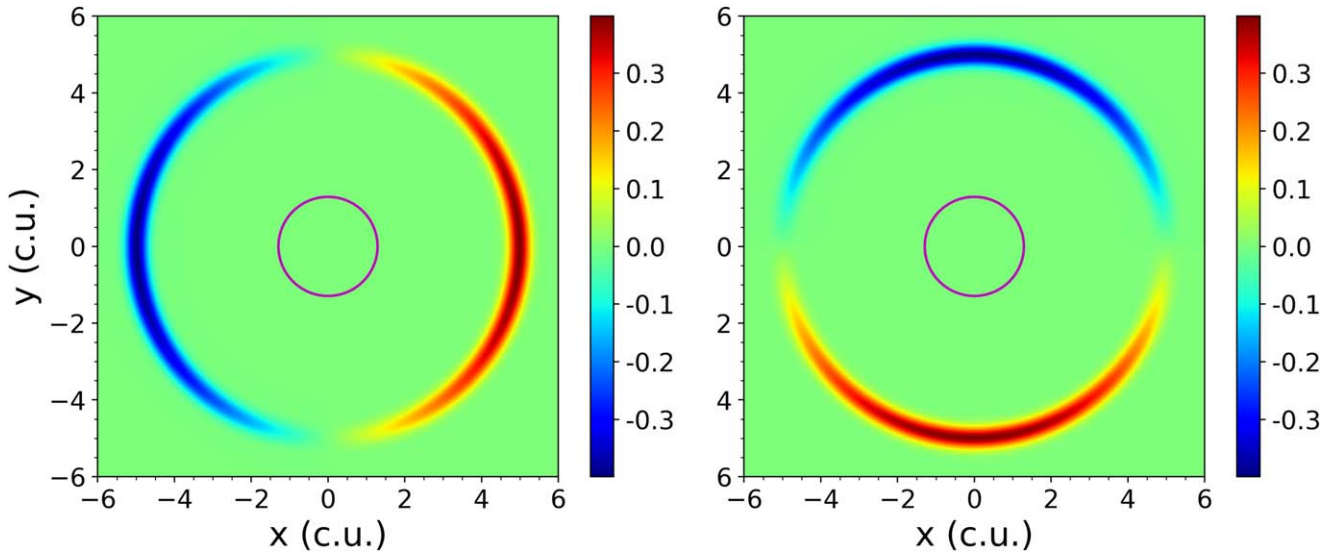


Figure 2. 2D profiles of the v_x and v_y velocity components of the initial circular pulse. The magenta-colored circle is the equipartition layer for a 1 MK coronal plasma. All values are depicted in code units.

given in code units:

$$n_d = 1.0005 + 0.0005 \tanh(r - r_d), \quad t > t_C, \quad (14)$$

where t_C is the time that we switch off the outward propagating pulse in the previous step and r_d being the effective distance from the null point at which the scheme starts acting. The value for r_d changes for each setup, to better accommodate the effects of the different Alfvén speed and speed of sound profiles for each setup and to make the dissipation of the reflective waves more effective.

Finally, for some of our setups we introduce explicit physical viscosity in the MHD equations, in addition to the previous numerical dissipation scheme (see also Karampelas et al. 2022b), with coefficient in code units:

$$n_{\text{visc}} = 0.1 + 0.1 \tanh(r - r_d), \quad t > t_C. \quad (15)$$

3. Results

The purpose of this study is to gain a better understanding of the nature of oscillatory reconnection in a hot coronal plasma and to explore its behavior under different coronal conditions. To that end, we expand the results of Karampelas et al. (2022a) through a series of parameter studies. For each parameter study, we change either the characteristic strength of the magnetic field, the equilibrium density, or the initial temperature. Studies of different magnetic fields and densities have been performed both in the absence and presence of anisotropic thermal conduction, whereas the study of the parameter of the temperature has been performed only in setups without thermal conduction. An overview of the different cases can be found in Table 1.

The initial velocity perturbation described by Equations (12) and (13) splits into two counter-propagating pulses of equal amplitude, with each traveling to opposing directions. While we deal with the outward propagating pulse in the way that was described in the previous section, we focus on the evolution and effects of the pulse approaching the null point. The inward propagating pulse focuses at the X-point due to refraction, as shown in Figure 3 for the default setup without thermal conduction ($B_0 = 1$, $\rho_0 = 1$, and $T = 1$ MK, see Model 2 in

Table 1). Mode conversion takes place as the fast magnetoacoustic wave pulse crosses the equipartition layer, from the region of low- β to the region of high- β plasma (e.g., McLaughlin & Hood 2006; Karampelas et al. 2022a), deforming the layer in the process due to the formation of strong compression and rarefaction shocks in the y -direction and x -direction, respectively (see also Gruszecki et al. 2011).

Once the pulse reaches the null point, it perturbs it from its equilibrium, forcing it to perform a series of reconnection events, which are characterized by a periodic manifestation of horizontal and vertical current sheets (i.e., oscillatory reconnection). Like in the past studies, our main tool for studying oscillatory reconnection will be the tracking of the oscillating J_z current density at the perturbed null point, as was first performed by McLaughlin et al. (2009), and the calculation of its period for each different case.

3.1. Magnetic Field Dependence

Our first goal is to revisit the effects of the characteristic strength of the magnetic field (B_0) on the oscillatory reconnection of an X-point in a hot coronal plasma. A first study has been performed in Karampelas et al. (2022a), for an X-point in the presence of anisotropic thermal conduction. Here we repeat this analysis for the updated numerical dissipation scheme that was first introduced in Karampelas et al. (2022b). The latter is more efficient in dealing with the reflections returning to the perturbed null point and thus leads to less contamination of the J_z current density signal and a cleaner resulting spectrum. Unlike the previous parameter study on the magnetic field strength (see Karampelas et al. 2022a), here we expand the analysis for setups both in the presence and absence of anisotropic thermal conduction. In total, we consider four different values for the characteristic strength of the magnetic field (0.5, 1, 2, and 3 B_0 , where $B_0 = 1.44$ G). We note here that the magnitude of the magnetic field is proportional to the radius for the X-point, and that the characteristic value of the field is not the maximum value in our setups. As can be seen in Table 1 for Models 1–4, in these four cases the initial density and temperature are $1 \rho_0 = 10^{-12} \text{ kg m}^{-3}$ and $1 T_0 = 1 \text{ MK}$, and we consider both the numerical dissipation scheme and a nonzero

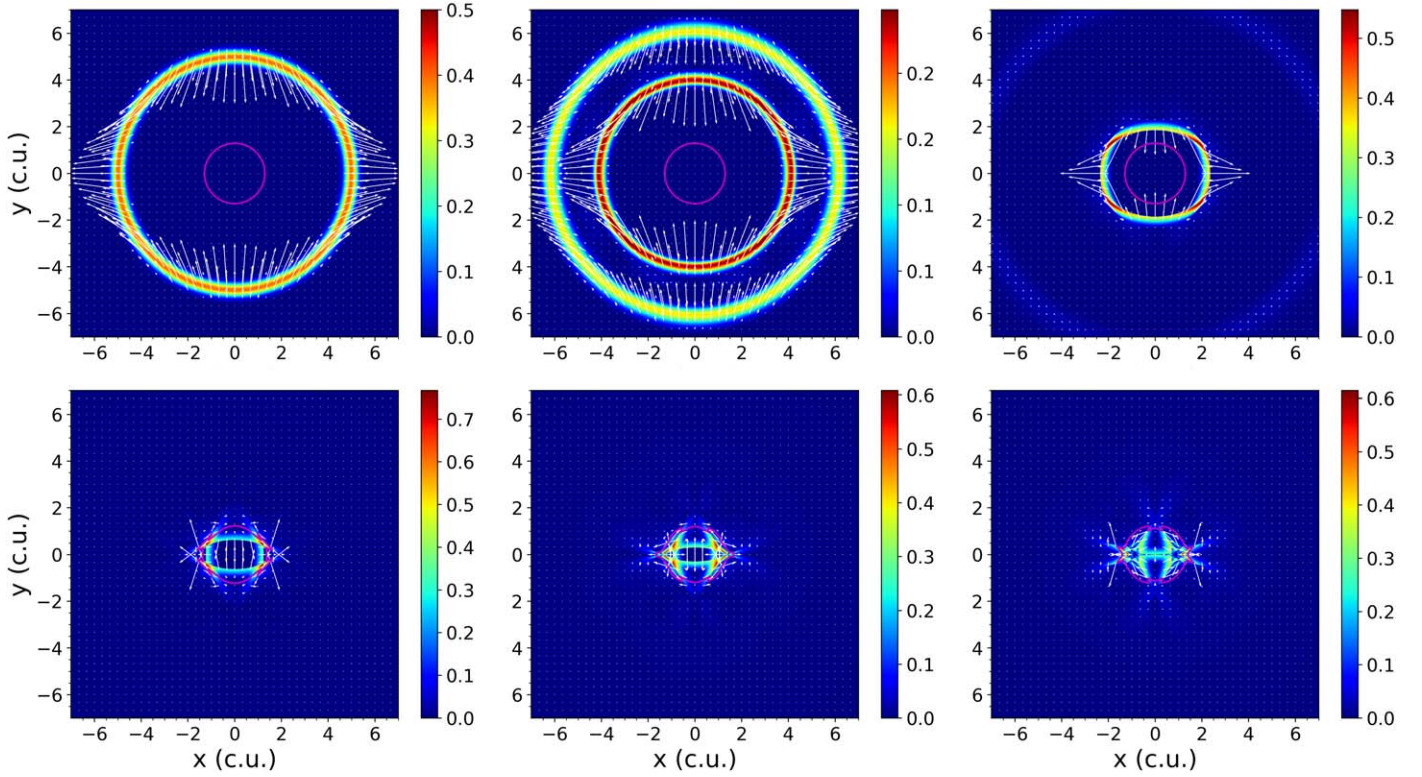


Figure 3. The evolution of the absolute value of the radial velocity for Model 2 (see Table 1), and the respective vector plot (normalized). Starting from the top, from left to right, the snapshots correspond to time $t = 0, 0.2, 0.8, 1.4, 1.6,$ and $1.8 t_0$. All values are depicted in code units.

Table 1

An Overview of the Physical Parameters (in Code Units) for the Different Models in Our Simulations

| Model | $B(B_0)$ | $\rho(\rho_0)$ | $T(T_0)$ | $\kappa_{\perp}, \kappa_{\parallel}$ | n_{visc} | $r_d(L_0)$ |
|-------|----------|----------------|----------|--------------------------------------|-------------------|------------|
| 1 | 0.5 | 1.0 | 1.0 | 0, $\neq 0$ | $\neq 0$ | 6 |
| 2 | 1.0 | 1.0 | 1.0 | 0, $\neq 0$ | $\neq 0$ | 5 |
| 3 | 2.0 | 1.0 | 1.0 | 0, $\neq 0$ | $\neq 0$ | 6 |
| 4 | 3.0 | 1.0 | 1.0 | 0, $\neq 0$ | $\neq 0$ | 6 |
| 5 | 1.0 | 2.0 | 1.0 | 0, $\neq 0$ | $\neq 0$ | 6 |
| 6 | 1.0 | 3.0 | 1.0 | 0, $\neq 0$ | $\neq 0$ | 6 |
| 7 | 1.0 | 4.0 | 1.0 | 0, $\neq 0$ | $\neq 0$ | 6 |
| 8 | 1.0 | 1.0 | 1.0 | 0 | 0 | 5 |
| 9 | 1.0 | 1.0 | 3.0 | 0 | 0 | 5 |
| 10 | 1.0 | 1.0 | 5.0 | 0 | 0 | 6 |
| 11 | 1.0 | 1.0 | 7.0 | 0 | 0 | 6 |
| 12 | 1.0 | 1.0 | 10.0 | 0 | 0 | 6 |

Note. Models 1–7 have been studied for both without ($\kappa_{\perp}, \kappa_{\parallel} = 0$) and with ($\kappa_{\perp}, \kappa_{\parallel} \neq 0$) anisotropic thermal conduction.

viscosity coefficient (n_{visc}) away from the null, in order to deal with the reflective waves.

The produced time series for the J_z current density of the different cases are shown in Figure 4, where the results both with and without thermal conduction are shown. Upon a visual inspection, we can see that in all cases oscillatory reconnection has developed, as is hinted by the oscillatory J_z signal at the null. The time series reveal for a stronger, and therefore stiffer magnetic field, the phenomenon of oscillatory reconnection lasts for progressively shorter times, before the oscillation is damped. This is in agreement with Karampelas et al. (2022a), where it was shown that the decay rates of these oscillations increase for stronger magnetic fields. On that note

and to reduce the computational costs, the simulations for 2 and 3 B_0 are left running only up to $t = 40 t_0$, since the oscillation decays faster than in the other cases. In the same study, it was also shown that the period of the oscillation also decreases for stronger, stiffer magnetic fields. This can also be derived from Figure 4, once we focus on the calculated wavelet spectra for each case, shown here below their respective time series. As can be seen, there is a clear trend regarding the period of the oscillation, with the dominant period band being shifted toward smaller values for stronger fields. Finally, we see that for most of the cases studied here, the dissipation scheme used to deal with the reflected waves is working efficiently, allowing us to produce clear spectra, where there is one clearly defined band of periods. The only exception is for the case of $0.5 B_0$ without anisotropic thermal conduction, where a strong secondary band of periods is observed. In Karampelas et al. (2022a) and Karampelas et al. (2022b) it was shown that these secondary period bands are associated with the reflected waves returning to the null point. This means that for this particular case, with the $0.5 B_0$ characteristic magnetic field strength, our dissipation scheme was less effective than in the other cases. However, the main period band is still clearly defined and more prominent than the other one.

In order to quantify this trend, we use the wavelet spectra to calculate the oscillation period for each case. We do so by first locating the coordinates (time t_0 and period P_0) of the maximum power for each spectrum. We then consider a time interval $\Delta t = [t_0 - P_0, t_0 + 3 P_0]$ containing the periods that exhibit higher values of power, for which we calculate the average value for the period, and the standard deviation, which will act as the error in the calculation. The calculated average values for the period of each oscillating signal are then placed in the graph of period versus the magnetic field strength, shown

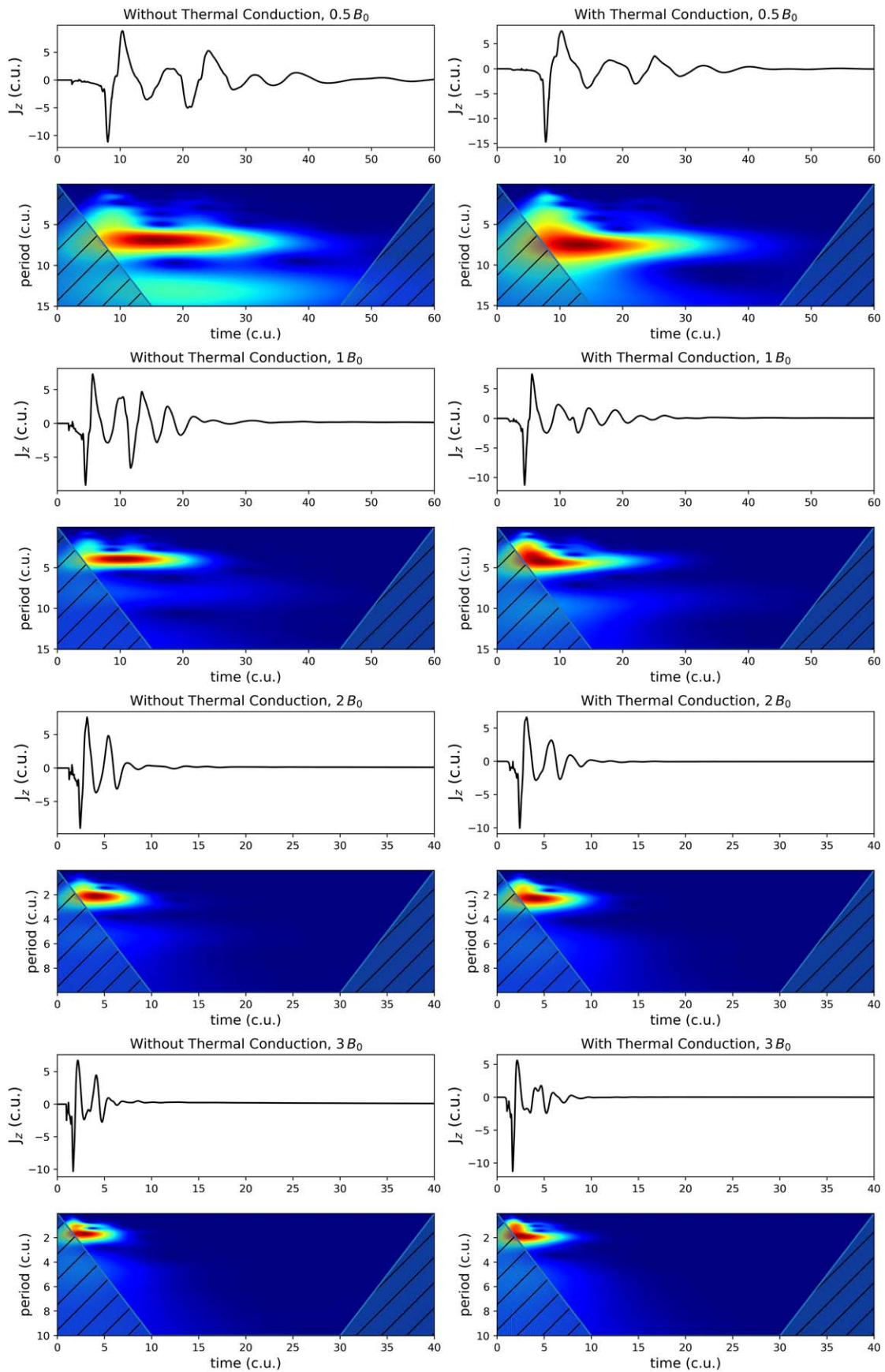


Figure 4. Time series of the J_z current density at the null point for setups with different characteristic magnetic field strengths (0.5 , 1 , 2 , and $3 B_0$). The equilibrium density and temperature are $1 \rho_0$ and 1 MK , respectively. Cases without (left column) and with anisotropic thermal conduction (right column) are considered. All values are depicted in code units.

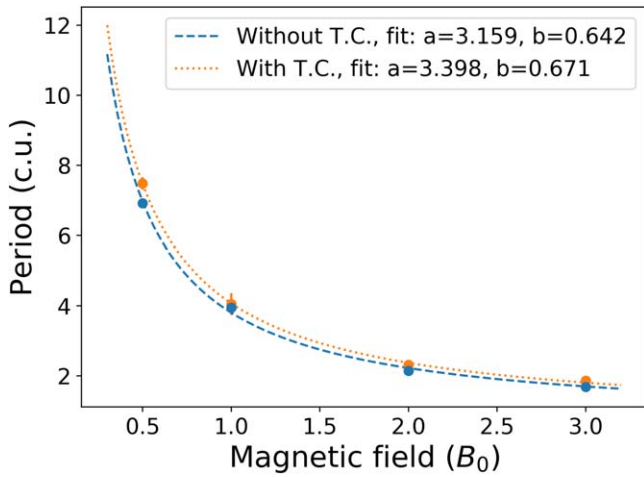


Figure 5. Graph depicting the distribution of the J_z oscillation period with respect to the magnetic field magnitude at radius $r = 1$. Overplotted are the fits for both distributions of the function $F(B_0) = a(B_0)^{-1} + b$. The blue-dashed and orange-dotted lines correspond to the cases without and with anisotropic thermal conduction. All values are depicted in code units, unless stated otherwise.

in Figure 5. The calculated standard deviation for each value is added as error bars for each point, although for most cases these error bars are barely visible. The data points shown in Figure 5 clearly hint toward an inverse proportionality relation between the oscillation period and the magnetic field strength. Because of this, we have fitted both sets of data points (with thermal conduction, in orange, and without thermal conduction, in blue) with the function $F(B_0) = a(B_0)^{-1} + b$. Figure 5 also shows the values of the coefficients for both cases, which are $a = (3.159 \pm 0.096, 3.398 \pm 0.046)$ and $b = (0.642 \pm 0.111, 0.671 \pm 0.053)$ for the cases without and with thermal conduction, respectively. We can see that the addition of thermal conduction does not alter the trend in any significant way. We can also see that the setups with thermal conduction generally give higher values of the period than those cases without thermal conduction, in agreement with our past studies (Karampelas et al. 2022a, 2022b).

3.2. Density Dependence

Our next goal is to study the response of oscillatory reconnection for different equilibrium densities. We have considered again four different cases, where we take density values $\rho = 1, 2, 3,$ and $4 \rho_0$ where $\rho_0 = 10^{-12} \text{ kg m}^{-3}$. In all cases, we have taken a characteristic strength of the magnetic field equal to $1 B_0 = 1.44 \text{ G}$, and temperature $1 T_0 = 1 \text{ MK}$. All cases are studied both in the presence and absence of anisotropic thermal conduction. Just like before, we again consider both the numerical dissipation scheme and a nonzero viscosity coefficient (n_{visc}) away from the null, to treat the reflections. The details of the different models (2, 5, 6, and 7) are shown in Table 1.

The derived time series for the J_z current density are shown in Figure 6 alongside their respective wavelet spectra. Again, the spectra of the time series reveal a prominent period band for each case, associated with the oscillatory reconnection process, the secondary period bands from the reflected waves being of lower power. Again, upon a visual inspection we can see that by increasing the value of the equilibrium density, the resulting

period of the oscillation increases as well, again with thermal conduction leading to higher periods.

Following the same process as in the previous case, we derive the average values for the period, and the errors from the standard deviation for each case and we place them in the same oscillation period-density graph, in Figure 7. Again, we can see a clear trend for each set of data points (with and without thermal conduction, shown in orange and blue, respectively). For each set of data points, we fit the function $G(\rho_0) = a(\rho_0)^{1/2} + b$, which we believe shows the best agreement with the observed trend of the values of the period. The values of the coefficients, as derived from the fit, are $a = (3.309 \pm 0.303, 3.352 \pm 0.190)$ and $b = (0.484 \pm 0.479, 0.602 \pm 0.300)$ without and with thermal conduction, respectively, and are also shown Figure 7.

3.3. Temperature Dependence

The final parameter study that we want to perform revolves around the response of oscillatory reconnection to the initial background temperature. In the previous subsection, we took setups of different background densities, but we kept the temperature the same for all cases, meaning that the speed of sound was always the same for those cases. In this section, we consider setups with different temperatures, and therefore different speeds of sound as well. We have considered five different cases, corresponding to Models 8–12 in Table 1. In all models, we have taken a characteristic strength of the magnetic field equal to $1 B_0 = 1.44 \text{ G}$, and an initial density of $1 \rho_0 = 10^{-12} \text{ kg m}^{-3}$, while the temperature takes values of 1, 3, 5, 7, and 10 MK. Unlike the two previous parameter studies, no anisotropic thermal conduction is considered in this one. This is due to the ever-increasing computational costs once thermal conduction is considered, caused by a combination of the increasing temperatures and the Alfvén speed profile for our given magnetic field geometry, making these simulations very costly to perform for the proper resolution. Additionally, for these five cases viscosity has been dropped from the artificial dissipation scheme dealing with the reflections. The viscous scheme did not work efficiently for the cases with higher temperatures and so we decided to drop it from the setups with lower temperatures, for consistency.

Figure 8 shows the produced times series of the J_z current density profiles at the perturbed null point, and the corresponding wavelet spectra for each profile. Unlike before, the changes in period here seem to be more subtle from one setup to the next. We see the gradual appearance of a secondary period band, which becomes increasingly stronger for higher temperatures, but without ever reaching the same power as the main period band. Given the more uneven J_z signal for higher temperatures, it is safe to associate this secondary period band with the reflected waves from the boundaries, polluting the null point region and giving rise to more noisy signals.

Following the same methodology as before for the magnetic field and the density, we again calculate the average values for the period of each case, and their respective errors through the standard deviation, and we plot them together in a graph, showing the relation between the period of oscillation and the background temperature. The results are shown in red in both panels of Figure 9. In the left panel, just like before, we also fit the function $F(T_0) = a(T_0)^{-1} + b$, with the coefficients taking the values $a = 0.743 \pm 0.060$ and $b = 3.532 \pm 0.029$. Although the fitted function passes through all the data points if we

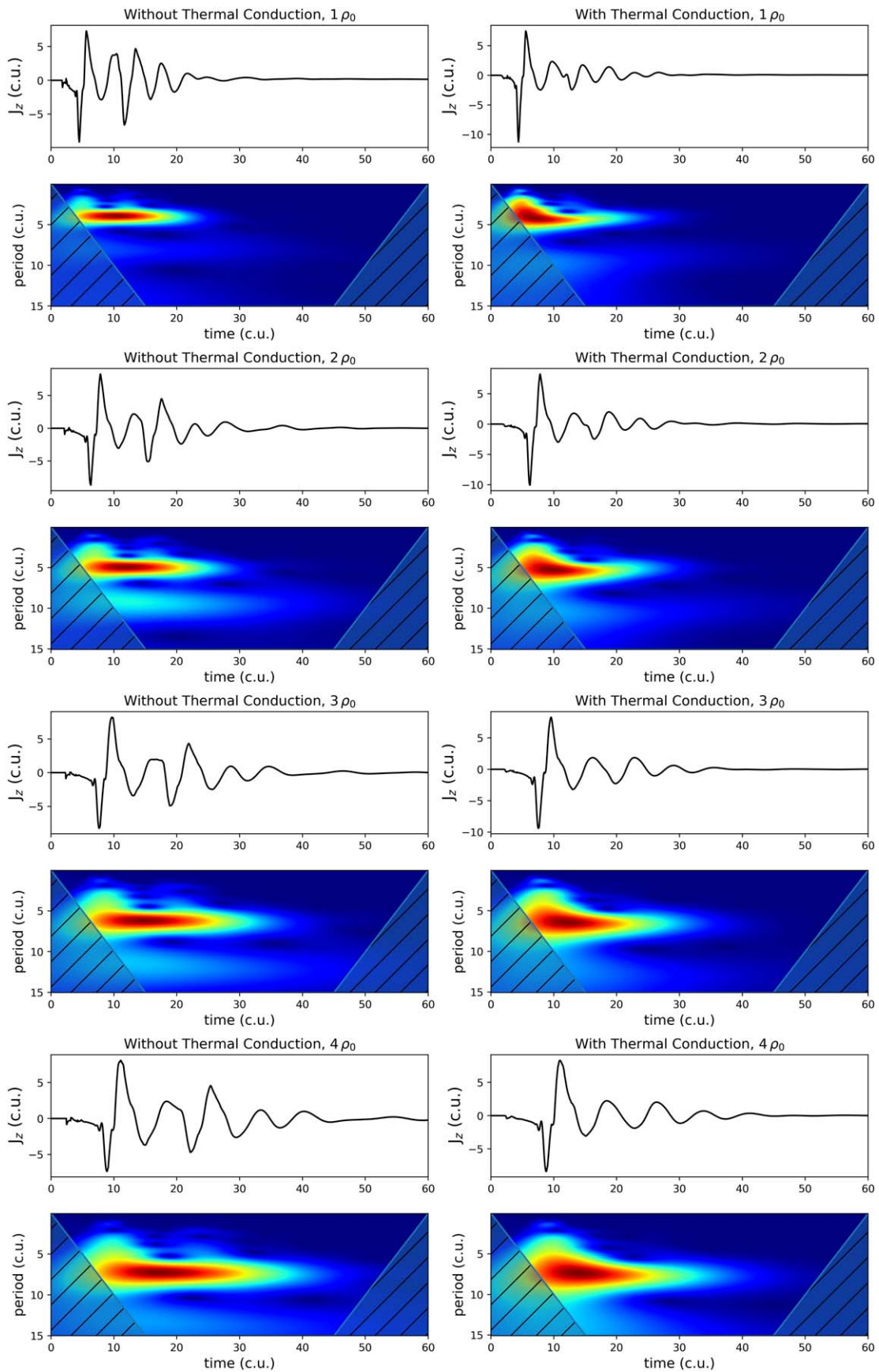


Figure 6. Time series of the J_z current density at the null point for setups with different equilibrium densities ($\rho = 1, 2, 3,$ and $4 \rho_0$). The equilibrium magnetic field magnitude at a radius of $r = 1$ and temperature are $1 B_0$ and 1 MK , respectively. Again, cases without (left column) and with anisotropic thermal conduction (right column) are considered. All values are depicted in code units.

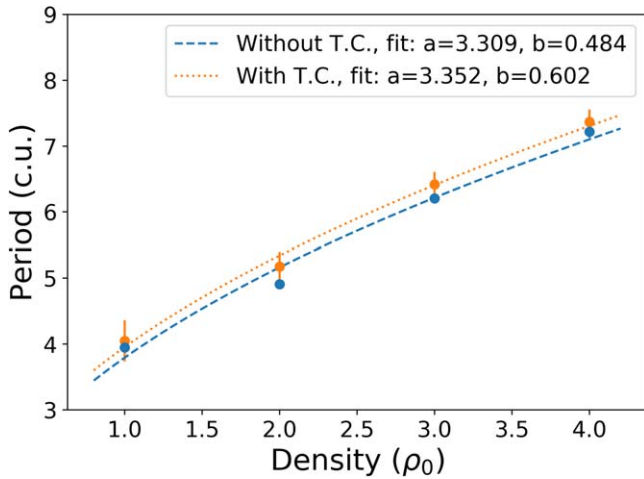


Figure 7. Same as Figure 5, but here we depict the oscillation period with respect to the background density. Overplotted are the fits for both distributions of the function $G(\rho_0) = a(\rho_0)^{1/2} + b$.

consider their error bars, we have also decided to fit the function $H(T_0) = a(T_0)^{-1/2} + b$ in our data (right panel), with coefficients $a = 1.02 \pm 0.013$ and $b = 3.241 \pm 0.007$. As can be seen by comparing both panels of Figure 9, the function $H(T_0)$ provides a better fit on the given data, with the coefficients presenting smaller errors in comparison to those for $F(T_0)$. Therefore, from now on we will use the $H(T_0) = a(T_0)^{-1/2} + b$ function to describe the dependency of the period on the background temperature. Also, it becomes obvious that for our range of chosen temperatures that match the coronal conditions, the variations of the period are considerably smaller than in the other case that we have examined.

Finally, we need to address the effects of the different dissipation schemes used in this parameter study. As mentioned earlier, for the cases considered in this subsection we took the numerical dissipation scheme described by the coefficient of Equation (14), without the supplementary viscous scheme described by the coefficient of Equation (15). In other words, for Models 8–12 in Table 1, we took $n_{\text{visc}} = 0$. When comparing the resulting periods for Model 2 ($P = 3.947 \pm 0.022$), used in the previous two subsections, and from its equivalent Model 8 used here ($P = 4.259 \pm 0.155$), we can see that the two produce slightly different results. It is not certain how removing the artificial viscous scheme leads to this small difference in period, of the order of $\Delta P \approx 0.312 t_0 = 2.43$ s. It is very likely that we are dealing with some code-specific numerical effects at this point, which would be hard to properly treat within the context of this study. However, the very small value of this difference makes us confident to compare our current results with those of the previous sections. To that end, we have subtracted the difference 0.312 from the periods for all of our data points shown in both panels of Figure 9. We do this because none of the cases studied in this subsection had the viscous dissipation scheme switched on and thus we have been consistent among these five different setups. The resulting adjusted points (in black) follow the same trend as before for each panel, with the fitted function $F(T_0)$ having coefficients $a = 0.743 \pm 0.060$ (same as before) and $b = (3.532 - 0.312) \pm 0.029 = 3.219 \pm 0.029$, and the fitted function $H(T_0)$ having coefficients $a = 1.02 \pm 0.013$ (same as before) and $b = 2.929 \pm 0.007$. We repeat that from now on we will be using the $H(T_0) = a(T_0)^{-1/2} + b$ function to

describe the dependency of the period on the background temperature.

4. Discussion and Conclusions

4.1. Parameter Studies

In this paper we once again revisit the mechanism of oscillatory reconnection of a 2D X-point in hot coronal plasma, further exploring its response to different coronal conditions. This is needed, due to the large number of observations that can be attributed to the process of oscillatory reconnection. The first step was taken in Karampelas et al. (2022a) where the periodicity and the decay rate of the mechanism were studied in the presence of anisotropic thermal conduction in coronal conditions, expanding past studies that focused on cold plasma. In that same study, a clear connection was revealed between the magnetic field strength and the period of the oscillation. The second step was taken in Karampelas et al. (2022b), where it was found that the period of oscillatory reconnection of a magnetic X-point perturbed by an external pulse is independent of the amplitude and type of the perturbing pulse. These two studies had already hinted toward the possibility of using oscillatory reconnection as a tool for coronal seismology. To that end, in the current study we have expanded upon the results of Karampelas et al. (2022a), by considering cases with different magnetic fields, densities, and background temperatures.

Our focus on the three quantities mentioned previously is based on the assumption that the properties of oscillatory reconnection, like its period, in the absence of dedicated external driving, should be related to the conditions of the background plasma in the vicinity of the null point. This is due to oscillatory reconnection being a fundamental process, related to the relaxation of a perturbed magnetic null point (here, X-point). Therefore, we do not expect the large-scale magnetic field topology to affect our results, as the field geometry used here is characteristic of the field geometry in the immediate neighborhood of an X-point. This is analogous to null points acting as resonant cavities (see Santamaria & Van Doorselaere 2018) where the wave-null point interaction properties are determined by the background plasma properties near the null point. Here we need to note that having external driving would lead to a dependency of the oscillation period on the period of the driving (Hegglund et al. 2009). However, our focus in this study is on the non-driven, relaxation-based oscillatory reconnection.

Using the PLUTO code, we have solved the compressible and resistive 2D MHD equations, for a series of parameter studies. The first one included four different setups, each for a different value of the characteristic strength of the magnetic field (0.5, 1, 2, and $3 B_0$, where $B_0 = 1.44$ G), studied both with and without anisotropic thermal conduction. We note here that the characteristic value of the field is not the same as its maximum value in each setup, rather the field magnitude is proportional to the distance from the X-point. The results revealed an inverse proportionality between the period and the strength of the magnetic field, as shown in Figure 5. In the second one, we considered again four different cases, where we took the density to be equal to $\rho = 1, 2, 3$, and $4 \rho_0$, where $\rho_0 = 10^{-12} \text{ kg m}^{-3}$, again studied both with and without anisotropic thermal conduction. The results, as shown in Figure 7, reveal a square root relation between the period and

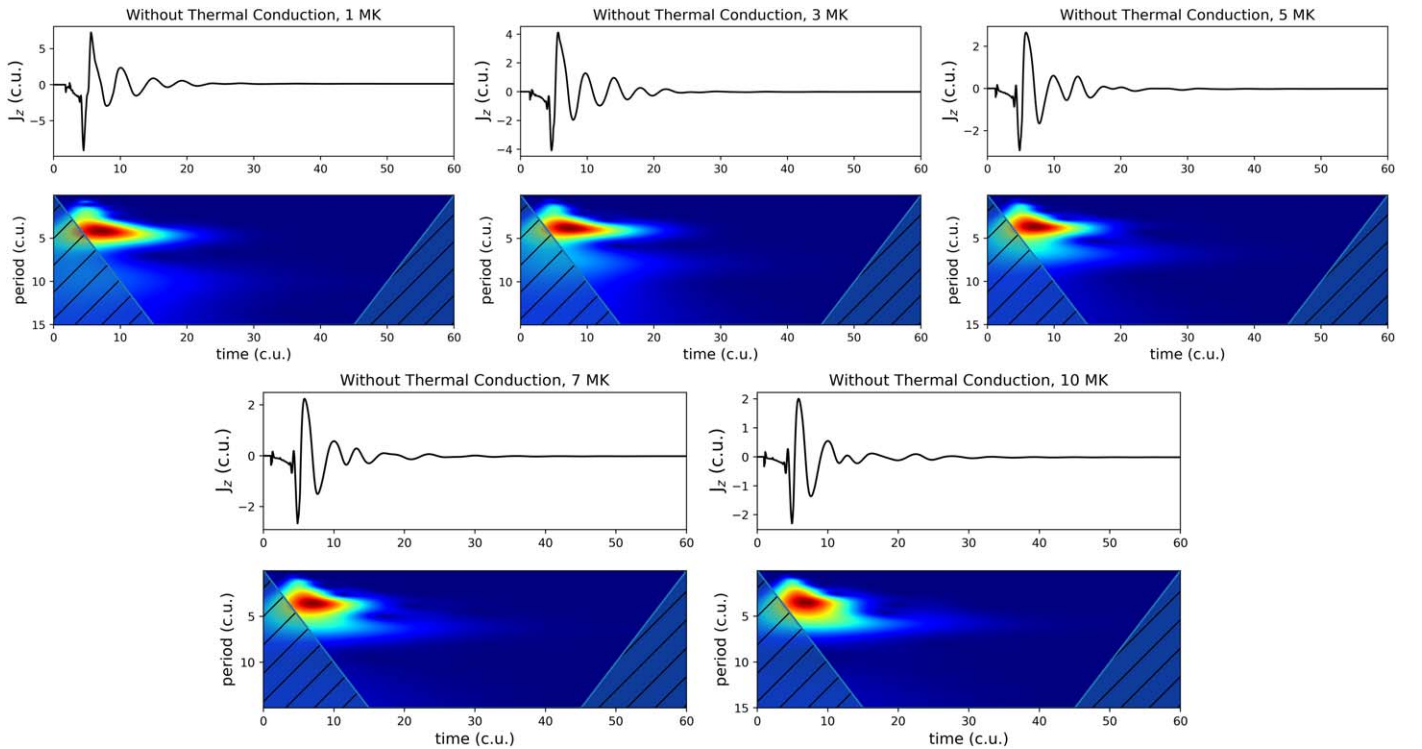


Figure 8. Time series of the J_z current density at the null point for setups with different equilibrium temperatures ($T = 1, 3, 5, 7,$ and 10 MK). The equilibrium magnetic field magnitude at a radius $r = 1$ and density are $1 B_0$ and $1 \rho_0$, respectively. Only setups without anisotropic thermal conduction are considered. All values are depicted in code units.

the equilibrium density. The third and final parameter study involved five setups with different values of background temperature (1, 3, 5, 7, and 10 MK), all studied in the absence of anisotropic thermal conduction. This last parameter study, shown in Figure 9, revealed an inverse proportional relation, this time between the period and the square root of the background temperature.

As expected from our previous studies, the cases with anisotropic thermal conduction practically follow the same trend as their respective ones without thermal conduction, their only difference being that the former exhibit slightly higher values of period. The only exception is for those setups in the temperature parameter study, where thermal conduction has not been considered, due to increased computational costs for our given resolution. This is caused by a combination of the increasing temperatures and the given magnetic field geometry.

Also, as explained in the previous section, the derived values for the period from the temperature parameter study are shifted with respect to the rest, due to the slightly different artificial dissipation scheme, without any supplementary viscosity-based scheme that was used throughout it. Comparing the resulting periods of two equivalent setups, each with a version of the dissipation scheme, we get a difference of $\Delta P \approx 0.312 t_0 = 2.43$ s, which is of the order of $\sim 8\%$ from the value of $P \sim 30$ s that we get from the other two parameter studies. Since we have used the same dissipation scheme when studying the response of oscillatory reconnection to temperature, we subtract ΔP from all of these results, as shown by the black line of the adjusted fit in both panels of Figure 9. This allows for a better comparison with the other two parameter studies presented here. A synopsis of the fitted functions and the values of their coefficients can be found in Table 2.

4.2. Period versus the Alfvén Speed and Speed of Sound

Continuing on the trend set by our analysis so far, we want to study the evolution of the period of oscillatory reconnection in terms of the Alfvén speed and speed of sound profiles. The initial Alfvén speed profile is dependent both on the initial equilibrium density and the characteristic magnetic field strength. We then take the results from the first seven models in Table 1, for the different values of density and characteristic magnetic field strength, calculate the characteristic Alfvén speed and plot them with respect to the period. This graph is shown in the left panel of Figure 10. We again fit the function $F(V_A) = a(V_A)^{-1} + b$, the coefficients of which take values of $a = (0.911 \pm 0.027, 0.941 \pm 0.020)$ and $b = (0.574 \pm 0.136, 0.672 \pm 0.103)$ for the data sets without and with thermal conduction, shown in blue-dashed and orange-dotted lines. This fit for the Alfvén speed is in agreement with the previous fits for the magnetic field and the density since the Alfvén speed is proportional to the magnetic field and inversely proportional to the square root of density. The right panel of the same figure, shows the results for the speed of sound, which are derived from those of the temperature parameter study without thermal conduction. In that panel, we show both the original values of the period (points in red) and the adjusted ones (points in black) for which we subtracted the difference $\Delta P \approx 0.312 t_0 = 2.43$ s as was mentioned in the section for the temperature parameter study. Finally, we fitted the function $F(V_S) = a(V_S)^{-1} + b$, for the original (red-dashed line) and the adjusted data (black-dotted line), the coefficients of which take values of $a = (1.317 \pm 0.016, 1.317 \pm 0.016)$ $b = (3.241 \pm 0.007, 2.929 \pm 0.007)$ for the original and adjusted data, respectively. This fit agrees with the one of the $H(T_0) = a(T_0)^{-1/2} + b$ function for the background temperature, presented in Section 3.3, since the speed of

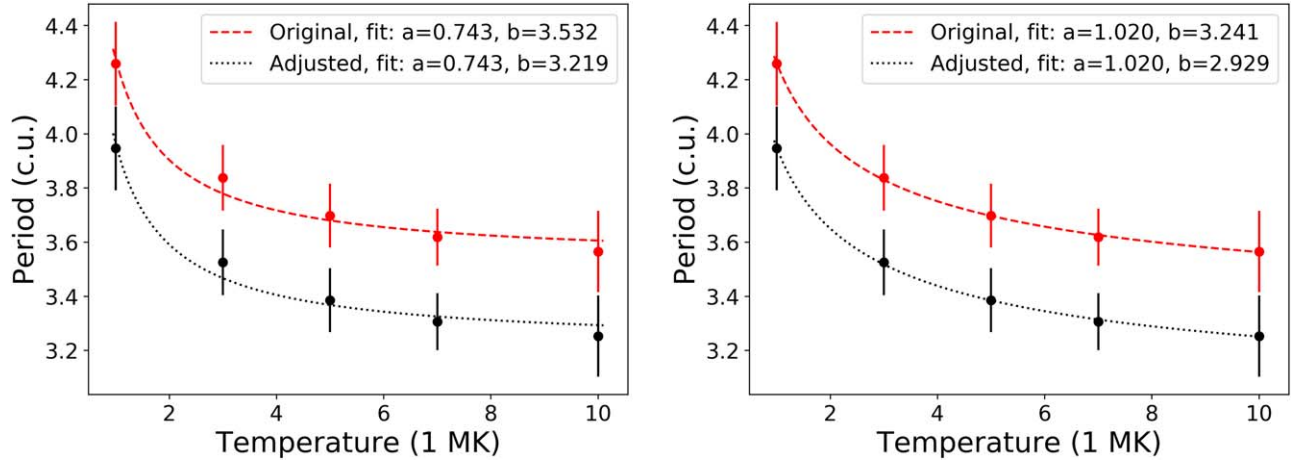


Figure 9. Graph depicting the distribution of the J_z oscillation period with respect to the equilibrium temperature. In the left panel, we fit the function $F(T_0) = a(T_0)^{-1} + b$ to our original data points (red-dashed line) and to the adjusted data points (black-dotted line). In the right panel, we do the same but for the function $H(T_0) = a(T_0)^{-1/2} + b$. All setups are considered in the absence of thermal conduction. All values are depicted in code units, unless stated otherwise.

Table 2

Summary of the Fitted Functions and the Values of Their Coefficients for the Parameter Studies, as Well as for the Alfvén Speed and Speed of Sound

| Study | Fit | a, b | |
|----------------|-------------|----------------|---------------------|
| | | (without T.C.) | (with T.C.) |
| Magnetic field | $F(B_0)$ | 3.159, 0.642 | 3.398, 0.671 |
| Density | $G(\rho_0)$ | 3.309, 0.484 | 3.352, 0.602 |
| Temperature | $H(T_0)$ | 1.020, 3.241 | <i>1.020, 2.929</i> |
| Alfvén speed | $F(V_A)$ | 0.911, 0.574 | 0.941, 0.672 |
| Speed of sound | $F(V_S)$ | 1.317, 3.241 | <i>1.317, 2.929</i> |

Note. The three types of fitted functions are $F(x) = a(x)^{-1} + b$, $G(x) = a(x)^{1/2} + b$, and $H(x) = a(x)^{-1/2} + b$. For the temperature and speed of sound, both pairs of coefficients are without thermal conduction, with the second pair being for the adjusted data sets. This is indicated in italics.

sound is proportional to the square root of the temperature. This further justifies the use of function $H(T_0)$ to describe the relation between the period of oscillatory reconnection and the plasma temperature.

4.3. Empirical Formula

As a last step, we want to merge the derived relations from each of the three parameter studies into one. We do this because one of the main goals of this present study was to start developing its capabilities as a plasma diagnostic tool. To that end, we are aided by the results of Karampelas et al. (2022b), which allow us to ignore the strength of the perturbing pulse from this relation. Taking the cases without thermal conduction, we can merge the derived relations of each previous fit into the following formula for our four key parameters:

$$\frac{P_{\text{ph}}}{t_0} = \frac{3.159 B_0}{B_{\text{ph}}} + 3.309 \sqrt{\frac{\rho_{\text{ph}}}{\rho_0}} + 1.02 \sqrt{\frac{T_0}{T_{\text{ph}}}} - 3.541 \pm 0.434, \quad (16)$$

where the penultimate term on the right-hand side comes from solving the above equation for a known value of the period P_{ph} (in seconds). For this, we considered the resulting period for Model 2 ($P_{\text{ph}} = (3.947 \pm 0.022) t_0$). We also include the maximum error in the last term on the right-hand side that is derived from the different combinations of errors in the values

of P_{ph} and the coefficients of the fits. Here, the subscript ‘‘ph’’ refers to the physical quantities U_{ph} , as defined in Section 2.1. For the quantities in physical units, we have $U_{\text{ph}} = U U_0$, with U the quantities in code units and U_0 the normalization units. We used the adjusted results for the temperature parameter study, as explained earlier, while all the coefficients are given in code units. Using the normalization units defined in Section 2.1, we can rewrite the above formula in SI units, except for the magnetic field which is given in Gauss:

$$P_{\text{ph}} = \frac{35.39}{B_{\text{ph}}} + 25.74 \times 10^6 \sqrt{\rho_{\text{ph}}} + \frac{7.94}{\sqrt{T_{\text{ph}}}} - 27.55 \pm 3.38, \quad (17)$$

where we have the period P_{ph} (in seconds) for a known combination of B_{ph} (in Gauss), ρ_{ph} (in kilograms per cubic meters) and T_{ph} (in megakelvins). A similar analysis of the cases with added thermal conduction can be found in Appendix.

Finally, we show in Table 3 some examples of using the above formula to calculate the periods of oscillatory reconnection for different combinations of parameters for a flaring coronal plasma. One thing that needs to be stressed is that Equation (17) has been derived from a set of values that reflect the average conditions in the solar corona. As a result, we need to be cautious when extrapolating the above relation for values outside of that parameter space, as we may end up with nonphysical results. However, the derived relation can be a useful plasma diagnostic tool in coronal conditions, and needs to be tested further against observational periodic signals, which could be attributed to oscillatory reconnection. Such periodic signals in the solar atmosphere include, but are not limited to, QPPs of solar (e.g., Kupriyanova et al. 2016) and stellar flares (e.g., Broomhall et al. 2019), quasi-periodic chromospheric (e.g., De Pontieu et al. 2011) and coronal jets (e.g., Hong et al. 2019; Mandal et al. 2022), QFP magnetosonic wave from the eruption of a magnetic flux rope (e.g., Shen et al. 2018), and periodicities correlated with Type III radio bursts (Cattell et al. 2021). A detailed discussion of the different phenomena attributed to oscillatory reconnection has already been presented in Section 1. The fundamental nature of oscillatory reconnection in perturbed magnetic X-points

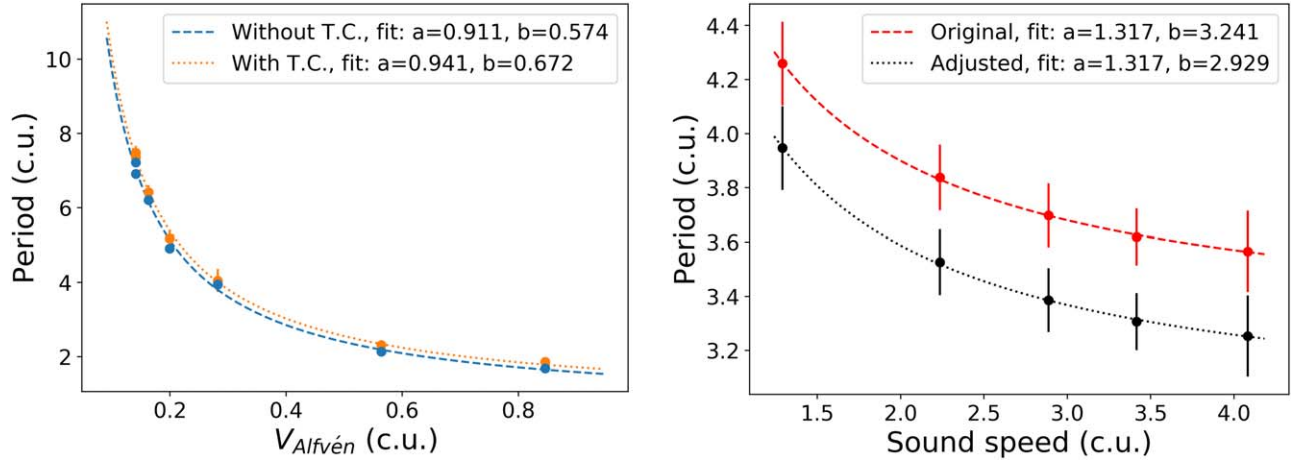


Figure 10. Left: oscillation period vs. the background Alfvén speed at radius $r = 1$, calculated for all the setups with the different background densities and equilibrium magnetic fields. The function $F(V_A) = a(V_A)^{-1} + b$ is fitted for both data sets. The choice of color shown in Figure 5 is also followed here. Right: same graph as in Figure 9, only now the background speed of sound is depicted instead of the background temperature. The function $F(V_S) = a(V_S)^{-1} + b$ is fitted for both data sets. All values are depicted in code units, unless stated otherwise.

Table 3

Examples of the Calculation of the Period of Oscillatory Reconnection through Equation (17)

| $B_{\text{ph}}(\text{G})$ | $\rho_{\text{ph}} (\text{kg m}^{-3})$ | $T_{\text{ph}}(\text{MK})$ | $P_{\text{ph}}(\text{s})$ |
|---------------------------|---------------------------------------|----------------------------|---------------------------|
| 10 | 2.0×10^{-12} | 5.0 | 15.9 |
| 20 | 2.0×10^{-12} | 5.0 | 14.2 |
| 30 | 2.0×10^{-12} | 5.0 | 13.6 |
| 20 | 2.0×10^{-12} | 3.0 | 15.2 |
| 20 | 2.0×10^{-12} | 10.0 | 13.1 |
| 20 | 3.0×10^{-12} | 5.0 | 22.4 |
| 20 | 5.0×10^{-12} | 5.0 | 35.3 |
| 20 | 30.0×10^{-12} | 5.0 | 118.8 |

Note. The subscript “ph” refers to the physical quantities $U_{\text{ph}} = U U_0$, with U the quantities in code units and U_0 the normalization unit (see also Section 2.1).

indicates that our derived plasma diagnostic tool can be employed to study the periodicities in the different cases of periodic signals attributed to oscillatory reconnection.

To summarize, our series of parameter studies have explored the effects of temperature, density, and magnetic field strength on the periodicity of oscillatory reconnection in a hot coronal plasma, expanding the earlier results of Karampelas et al. (2022a). Our findings show that the period of the oscillation depends on the underlying characteristics of the plasma near the null point. Taking into additional account the independence of the periodicity of oscillatory reconnection from the strength and type of the initial, perturbing pulse (Karampelas et al. 2022b), we have now developed a first quantitative formula to be used as a plasma diagnostic, opening the possibility of using this mechanism within the context of coronal seismology.

All authors acknowledge the UK Science and Technology Facilities Council (STFC) for support from grant No. ST/T000384/1. K.K. also acknowledges the support of an FWO (Fonds voor Wetenschappelijk Onderzoek - Vlaanderen) postdoctoral fellowship (1273221N). This work used the Oswald High Performance Computing facility operated by Northumbria University (UK).

Appendix

Empirical Formula for Added Thermal Conduction

In Section 4.3, we derived an empirical formula (see Equations (16) and (17)) that connects the period of oscillatory reconnection with the characteristic strength of the magnetic field, background density, and equilibrium plasma temperature. We did this by merging the derived relations of each fit in the data sets without the anisotropic conduction, discussed in Section 3. A similar formula can be derived for the period, magnetic field strength, and density when we include anisotropic thermal conduction for a plasma temperature of $T_{\text{ph}} = 1 \text{ MK}$:

$$\frac{P_{\text{ph}}}{t_0} = 3.398 \frac{B_0}{B_{\text{ph}}} + 3.352 \sqrt{\frac{\rho_{\text{ph}}}{\rho_0}} - 2.701 \pm 0.547, \quad (\text{A1})$$

where we used the period of Model 2 (see Table 1) with thermal conduction switched on ($P_{\text{ph}} = (4.049 \pm 0.311)t_0$) in order to calculate the penultimate term on the right-hand side. Similarly to Equation (16), we also include the maximum error derived from the different combinations of errors in the values of P_{ph} and the coefficients of the fits. When written in SI units, except the magnetic field, which is in Gauss, the previous relation takes the form

$$P_{\text{ph}} = \frac{38.07}{B_{\text{ph}}} + 26.08 \times 10^6 \sqrt{\rho_{\text{ph}}} - 21.01 \pm 4.26, \quad (\text{A2})$$

where we again take B_{ph} in Gauss and ρ_{ph} in kilograms per cubic meter, for $T_{\text{ph}} = 1 \text{ MK}$.

One drawback of the current study is the fact that, due to numerical reasons, implementing thermal conduction for the setups with high coronal temperatures ($>1 \text{ MK}$) leads to very costly and slow-to-perform simulations for our resolution of choice. That means that Equations (A1) and (A2) lack the temperature term of Equations (16) and (17) and can only be valid for plasma with temperatures near 1 MK. However, that might not necessarily hinder our analysis. By comparing the two sets of equations, we can see that the respective coefficients for each independent variable are very close in value to each other, when considering either the dimensionless or dimensionalized expressions, respectively. Also, from our

past studies (Karampelas et al. 2022a, 2022b) and the results of the parameter studies for the magnetic field and density, we know that the addition of thermal conduction only increases the values of the oscillation period by a small amount. Given that for $T=1$ MK, the parallel to the magnetic field thermal conduction coefficient κ_{\parallel} is already many orders of magnitude larger than the perpendicular one κ_{\perp} , it is unlikely that an increased temperature will significantly change the response of our setups to anisotropic thermal conduction. We thus conclude that our empirical formula without anisotropic thermal conduction (see Equations (16) and (17)) are accurate for solar coronal plasma.

ORCID iDs

Konstantinos Karampelas  <https://orcid.org/0000-0001-5507-1891>
 James A. McLaughlin  <https://orcid.org/0000-0002-7863-624X>
 Gert J. J. Botha  <https://orcid.org/0000-0002-5915-697X>
 Stéphane Régnier  <https://orcid.org/0000-0001-8954-4183>

References

- Bale, S. D., Badman, S. T., Bonnell, J. W., et al. 2019, *Natur*, **576**, 237
 Bale, S. D., Goetz, K., Harvey, P. R., et al. 2016, *SSRv*, **204**, 49
 Broomhall, A.-M., Thomas, A. E. L., Pugh, C. E., Pye, J. P., & Rosen, S. R. 2019, *A&A*, **629**, A147
 Brown, D. S., & Priest, E. R. 2001, *A&A*, **367**, 339
 Cattell, C., Glesener, L., Leiran, B., et al. 2021, *A&A*, **650**, A6
 Clarke, B. P., Hayes, L. A., Gallagher, P. T., Maloney, S. A., & Carley, E. P. 2021, *ApJ*, **910**, 123
 Craig, I. J. D., & McClymont, A. N. 1991, *ApJL*, **371**, L41
 De Pontieu, B., & McIntosh, S. W. 2010, *ApJ*, **722**, 1013
 De Pontieu, B., McIntosh, S. W., Carlsson, M., et al. 2011, *Sci*, **331**, 55
 Galsgaard, K., & Nordlund, Å. 1997, *JGR*, **102**, 231
 Gruszecki, M., Vasheghani Farahani, S., Nakariakov, V. M., & Arber, T. D. 2011, *A&A*, **531**, A63
 Guarcello, M. G., Micela, G., Sciortino, S., et al. 2019, *A&A*, **622**, A210
 Hayes, L. A., Inglis, A. R., Christe, S., Dennis, B., & Gallagher, P. T. 2020, *ApJ*, **895**, 50
 He, J., Zhu, X., Yang, L., et al. 2021, *ApJL*, **913**, L14
 Heggland, L., De Pontieu, B., & Hansteen, V. H. 2009, *ApJ*, **702**, 1
 Heyvaerts, J., & Priest, E. R. 1983, *A&A*, **117**, 220
 Hong, J., Yang, J., Chen, H., et al. 2019, *ApJ*, **874**, 146
 Jackman, J. A. G., Wheatley, P. J., Pugh, C. E., et al. 2019, *MNRAS*, **482**, 5553
 Jelinek, P., Karlicky, M., & Murawski, K. 2015, *ApJ*, **812**, 105
 Karampelas, K., McLaughlin, J. A., Botha, G. J. J., & Régnier, S. 2022a, *ApJ*, **925**, 195
 Karampelas, K., McLaughlin, J. A., Botha, G. J. J., & Régnier, S. 2022b, *ApJ*, **933**, 142
 Kasper, J. C., Bale, S. D., Belcher, J. W., et al. 2019, *Natur*, **576**, 228
 Kupriyanova, E., Kolotkov, D., Nakariakov, V., & Kaufman, A. 2020, *STP*, **6**, 3
 Kupriyanova, E. G., Kashapova, L. K., Reid, H. A. S., & Myagkova, I. N. 2016, *SoPh*, **291**, 3427
 Li, D., & Chen, W. 2022, *ApJL*, **931**, L28
 Li, D., Feng, S., Su, W., & Huang, Y. 2020a, *A&A*, **639**, L5
 Li, D., Ge, M., Dominique, M., et al. 2021, *ApJ*, **921**, 179
 Li, D., Lu, L., Ning, Z., et al. 2020b, *ApJ*, **893**, 7
 Li, D., Shi, F., Zhao, H., et al. 2022, *FrASS*, **9**, 1032099
 Longcope, D. W. 2005, *LRSP*, **2**, 7
 Mancuso, S., Barghini, D., & Telloni, D. 2020, *A&A*, **636**, A96
 Mandal, S., Chitta, L. P., Peter, H., et al. 2022, *A&A*, **664**, A28
 McLaughlin, J. A., De Moortel, I., Hood, A. W., & Brady, C. S. 2009, *A&A*, **493**, 227
 McLaughlin, J. A., & Hood, A. W. 2006, *A&A*, **459**, 641
 McLaughlin, J. A., Nakariakov, V. M., Dominique, M., Jelinek, P., & Takasao, S. 2018, *SSRv*, **214**, 45
 McLaughlin, J. A., Thurgood, J. O., & MacTaggart, D. 2012a, *A&A*, **548**, A98
 McLaughlin, J. A., Verth, G., Fedun, V., & Erdelyi, R. 2012b, *ApJ*, **749**, 30
 Mignone, A., Bodo, G., Massaglia, S., et al. 2007, *ApJS*, **170**, 228
 Mignone, A., Zanni, C., Tzeferacos, P., et al. 2012, *ApJS*, **198**, 7
 Murawski, K., Zaqarashvili, T. V., & Nakariakov, V. M. 2011, *A&A*, **533**, A18
 Murray, M. J., van Driel-Gesztelyi, L., & Baker, D. 2009, *A&A*, **494**, 329
 Nobrega-Siverio, D., & Moreno-Insertis, F. 2022, *ApJL*, **935**, L21
 Notsu, Y., Maehara, H., Honda, S., et al. 2019, *ApJ*, **876**, 58
 Orlando, S., Bocchino, F., Reale, F., Peres, G., & Pagano, P. 2008, *ApJ*, **678**, 274
 Parker, E. N. 1957, *JGR*, **62**, 509
 Petschek, H. E. 1964, in *Magnetic Field Annihilation*, ed. W. N. Hess, 50 (Washington, DC: NASA), 425
 Pugh, C. E., Nakariakov, V. M., Broomhall, A.-M., Bogomolov, A. V., & Myagkova, I. N. 2017, *A&A*, **608**, A101
 Ramsay, G., Kolotkov, D., Doyle, J. G., & Doyle, L. 2021, *SoPh*, **296**, 162
 Régnier, S., Parnell, C. E., & Haynes, A. L. 2008, *A&A*, **484**, L47
 Sabri, S., Ebadi, H., & Poedts, S. 2020, *ApJ*, **902**, 11
 Samanta, T., Tian, H., Yurchyshyn, V., et al. 2019, *Sci*, **366**, 890
 Santamaria, I. C., & Van Doorselaere, T. 2018, *A&A*, **611**, A10
 Shen, Y., Liu, Y., Song, T., & Tian, Z. 2018, *ApJ*, **853**, 1
 Shi, F., Ning, Z., & Li, D. 2022, *RAA*, **22**, 105017
 Shibata, K., & Magara, T. 2011, *LRSP*, **8**, 6
 Stewart, J., Browning, P. K., & Gordovskyy, M. 2022, *MNRAS*, **513**, 5224
 Sweet, P. A. 1958, in *IAU Symp. 6, Electromagnetic Phenomena in Cosmical Physics*, ed. B. Lehnert (Cambridge: Cambridge Univ. Press), 123
 Thurgood, J. O., Pontin, D. I., & McLaughlin, J. A. 2017, *ApJ*, **844**, 2
 Thurgood, J. O., Pontin, D. I., & McLaughlin, J. A. 2018a, *ApJ*, **855**, 50
 Thurgood, J. O., Pontin, D. I., & McLaughlin, J. A. 2018b, *PhPI*, **25**, 072105
 Thurgood, J. O., Pontin, D. I., & McLaughlin, J. A. 2019, *A&A*, **621**, A106
 Van Doorselaere, T., Kupriyanova, E. G., & Yuan, D. 2016, *SoPh*, **291**, 3143
 Vida, K., Olah, K., Kovari, Z., et al. 2019, *ApJ*, **884**, 160
 Xue, Z., Yan, X., Jin, C., et al. 2019, *ApJL*, **874**, L27
 Yuan, D., Feng, S., Li, D., Ning, Z., & Tan, B. 2019, *ApJL*, **886**, L25
 Yurchyshyn, V., Cao, W., Abramenko, V., Yang, X., & Cho, K.-S. 2020, *ApJL*, **891**, L21
 Zhang, Q. M., Chen, P. F., Ding, M. D., & Ji, H. S. 2014, *A&A*, **568**, A30
 Zimovets, I. V., McLaughlin, J. A., Srivastava, A. K., et al. 2021, *SSRv*, **217**, 66